Supporting Information

The Importance of Schottky Barrier Height in Plasmonically Enhanced Hot-Electron Devices

*Shenyou Zhao, Yanting Yin, Jun Peng, Yiliang Wu, Gunther G. Andersson, Fiona J Beck**

S1. Scanning Electron Microscopy (SEM) and X-ray Diffraction (XRD) Analysis

The crystallinity of TiO_2 was studied by SEM and XRD, and the results shown in Figure S1 and S2 demonstrate that the structure of ALD TiO_2 changes from amorphous to anatase phase with increasing deposition temperature from 200 ˚C to 300 ˚C. This suggests that amorphous TiO_2 could transform to crystalline TiO_2 with increasing deposition temperature. The diffraction peaks in Figure S2 could be attributed to anatase phase, with peaks at 25.4 ˚C and 48.14 ˚C corresponding to (101) and (200), respectively.

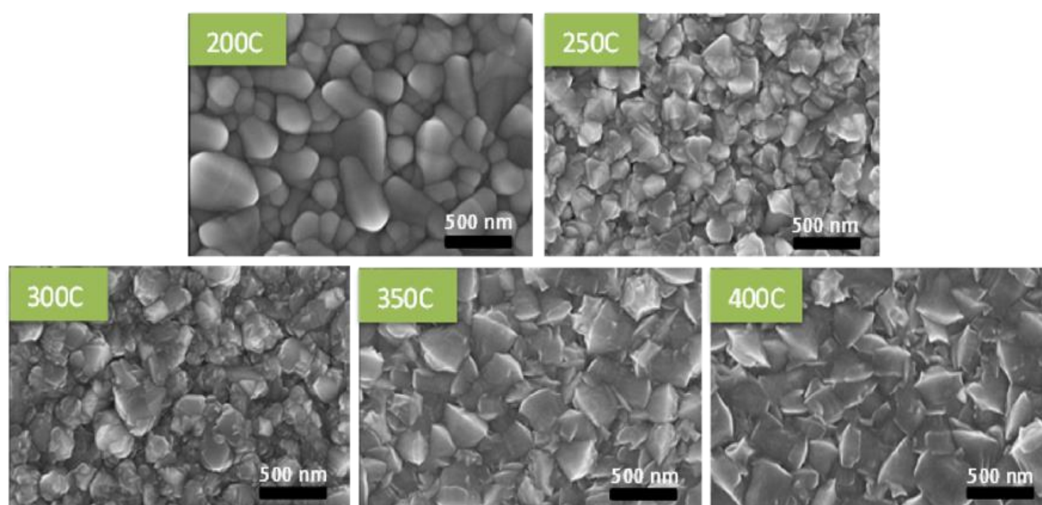

Figure S1 SEM images of ALD TiO_2 at various deposition temperatures. Scale: 500 nm.

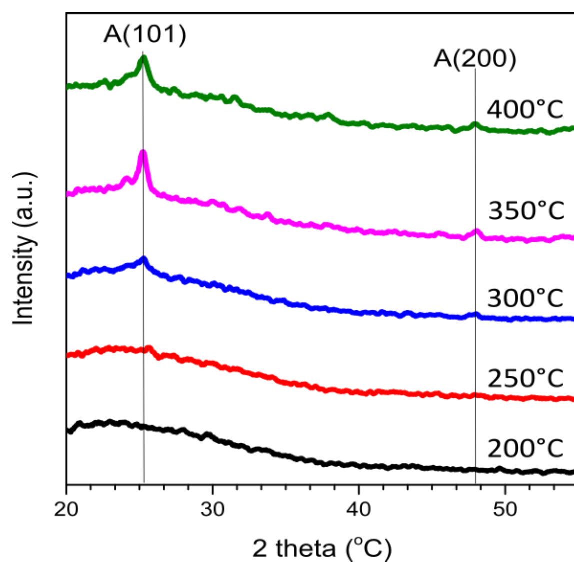

Figure S2 XRD for various TiO2 ALD deposition temperatures. The 'A' means anatase phase.

S2. UV/Visible Spectra of TiO_2/AuNPs/NiO and TiO_2

The absorption spectra of samples with various deposition temperatures were measured. Figure S3 shows that the absorption of 250 ˚C TiO_2 is higher than others below 550 nm (due to the smaller bandgap of 250 ˚C TiO_2 than others), whereas the absorption at resonance 620±10 nm of every TiO_2 does not have much difference from each other. The results indicate that the absorption of the samples at the LSPR is not strongly affected by ALD deposition temperature.

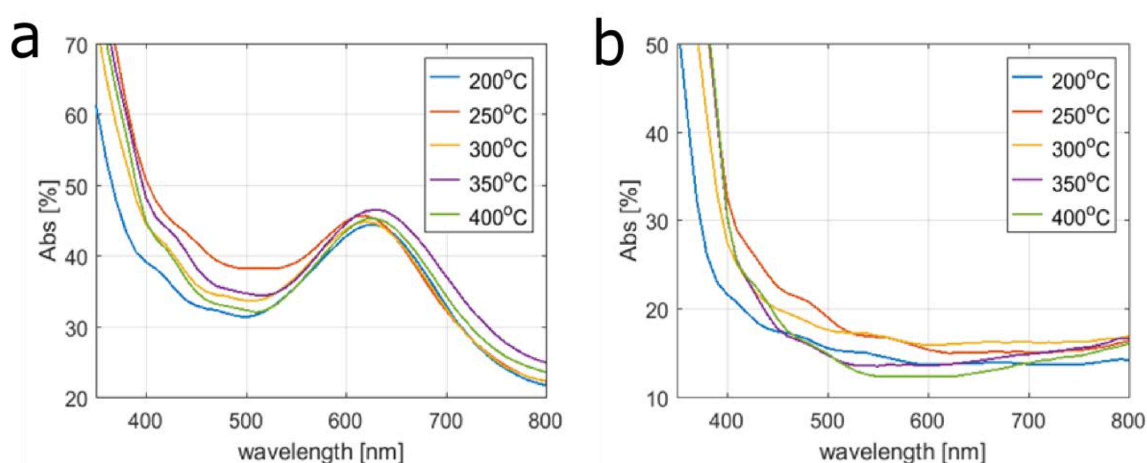

Figure S3 Absorption of various TiO2 ALD deposition temperatures. a) from bottom to top is FTO/TiO_2/AuNPs/NiO b) from bottom to top is FTO/TiO2.

S3. Current-Voltage Characteristics

Current-Voltage measurements were conducted both under dark and under filtered white light using a 550 nm optical longpass filter to avoid contributions to the short-circuit current density (J_{sc}) from direct TiO_2 excitation. The optical power of the filtered white light was around between 11 mW and 13 mW within the accuracy of the thermal power meter. Figure S4 shows the current density of the PEH devices as a function of applied voltage. The active area of the devices is 0.06 cm^2. The data shows that the J_{sc} of devices with TiO_2 deposited at 200°C is very small, while the J_{sc} of devices with TiO_2 deposited at 250°C is close to 0.05 mA/cm^2. As expected, the trend of the J_{sc} agrees with that of the EQE and has an overall decrease with increasing deposition temperature from 250°C to 400°C (shown in Figure S5), while the open-circuit voltage (V_{oc}) has an overall increase.

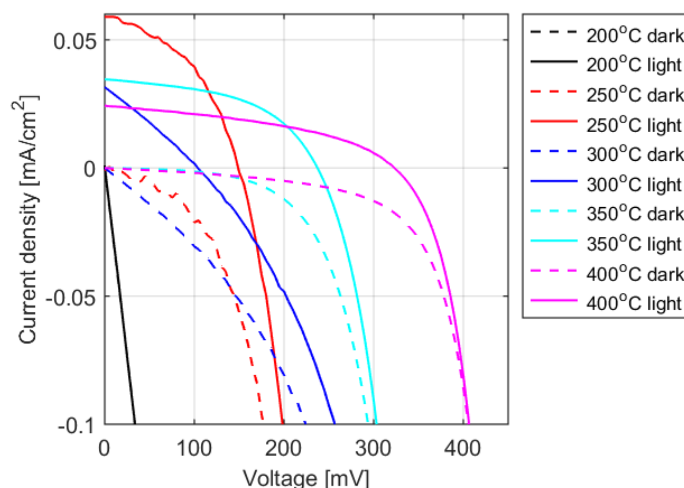

Figure S4 Current density of PEH and reference devices at various TiO_2 ALD deposition temperatures

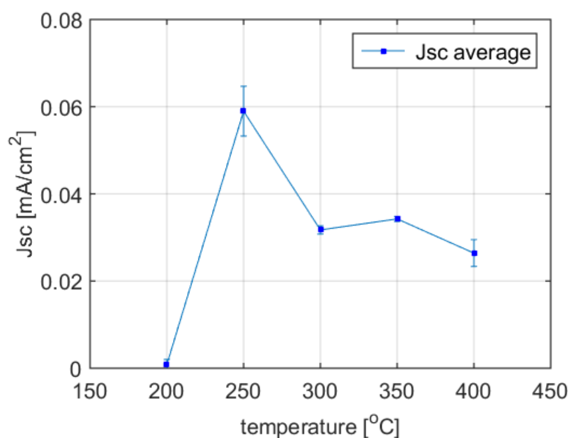

Figure S5 Short-circuit photocurrent (Jsc) of PEH devices as a function of TiO_2 ALD deposition temperature. The J_{sc} was averaged over at least 2 devices at each temperature.

S4. Linear Relationship between Intensity of Light and Photocurrent Density

The photocurrent density is linearly dependent on the intensity of incident light, so the short-circuit current measurements conducted on different dates can be compared as long as the incident optical powers are normalized. It is known that the rate of the charge separation depends linearly on the number of incident photons, namely the intensity of incident light. The linear relationship between the measured current density and the intensity of light indicates that the rate of charge recombination increases linearly with the rate of charge separation.

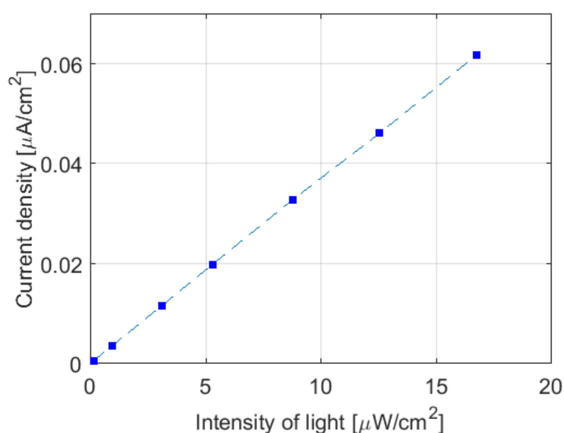

Figure S6 Photocurrent density generated by a PEH device is linearly dependent on the intensity of incident light. 600 nm monochromatic light was used for this measurement.

S5. Series Resistance of Schottky Diodes

The series resistance (Rs) was extracted from the IV-measurements using the method presented by Cheung.[1] Results show that 250-400°C samples have Rs = 35±5 Ω, but the amorphous TiO_2 deposited at 200°C has ~170 times higher resistance.

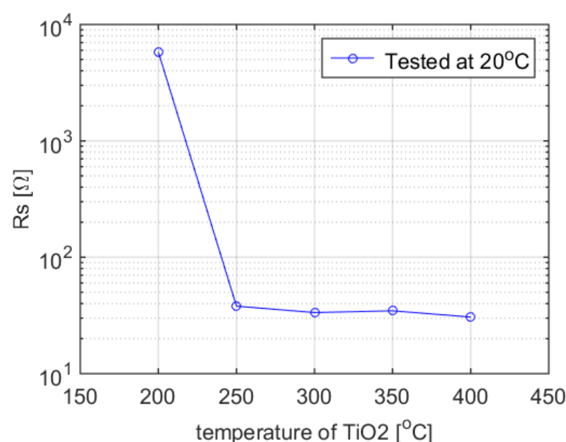

Figure S7 Series resistance (Rs) as a function of TiO2 ALD deposition temperature

From Figure S7, the Rs of 200 ˚C TiO_2 is much larger than others, which indicates its conductivity is very low and explains the reason for the low EQE of 200 ˚C TiO_2.

S6 Extracting Schottky Barrier Height by Current-VoltageMeasurements

Chueng's method can also be used to extract the SBH Schottky Barrier Height (SBH). [1] Figure S8 below shows an example of fitting the experimental data using Cheung's method, for one Au/TiO_2 diode with TiO2 deposited at 400 °C and the diode measured at 0 °C. Data were calculated assuming an area A = 0.06 cm^{-2} and the Richardson constant A* = 671 $Acm^{-2}K^{-2}$.

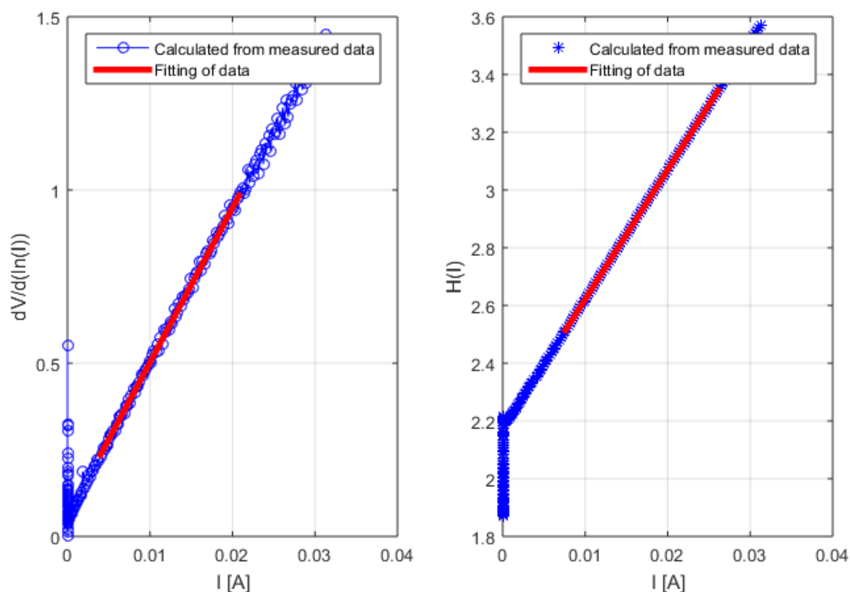

Figure S8 Fitting the experimental data using Cheung's method, for one Au/TiO_2 diode with TiO2 deposited at 400 °C.

The barrier height results for TiO2 deposited at different deposition temperatures are shown in the Table S1 below.

Tabel S1 Barrier height, ideality factor n, and surface roughness for TiO2 deposited on FTO glass at different temperatures

Deposition temperature of TiO2	**200°C**	**250°C**	**300°C**	**350°C**	**400°C**
SBH by Cheung method tested at 0 °C (different samples)	**0.73 eV** **0.74 eV**	**0.59 eV** **0.59 eV** **0.59 eV**	**0.59 eV** **0.60 eV** **0.61 eV**	**0.72 eV** **0.74 eV** **0.75 eV**	**0.81 eV** **0.86 eV** **0.88 eV**
n by Cheung method tested at 0 °C (different samples)	**17.8** **16.8**	**8.5** **8.8** **9.1**	**13.0** **12.1** **12.5**	**4.5** **4.2** **3.6**	**3.0** **2.6** **2.4**

Surface roughness estimated from SEM images	123.7 nm	154.6 nm	154.8 nm	142.7 nm	137.6 nm

The ideality factor (n) is a measure of the extent to which the PEH devices mesaued agree with ideal thermionic emission theory. Values of n larger than one mean that there are also other current transport mechanisms across the Schottky barrier, such as generation-recombination current. [2] The values of n larger than 2 indicate that the current is limited by current leakage, inhomogeneities of barrier, image force lowering of SBH, an insulating layer at the interface, surface states, series resistance, etc. [3-7]The main errors in this methods are from the effective device area A, due to the different surface roughness observed in the SEM images above, and the Richardson Coefficient, A* due to difference in the crystallinity of the TiO_2. Both of these could likely vary as a function of the deposition temperature.

The Richardson constant A* is dependent on the effective mass of the electrons in TiO2 and varies from 671 to 1200 $Acm^{-2}K^{-2}$ according to literature. [8-10] Uncertainty in A* would result in a error of roughly 0.02eV in barrier height.

It is more difficult to estimate the dependence of the effective device area on deposition temperature. The surface area is likely much larger than geometric area and dependent on the surface roughness of the TiO_2/FTO, whereas the electrically active area may be only a very small fraction of the surface area. The sample surface roughness is estimated from SEM images in Figure S1 and given in Table S1 above. While it is not possible to calculate the actual error in the effective area, we can see that the extracted SBH is strongly correlated with the surface roughness. For this reason, we do not consider these measurements accurate, and instead use photoelectron spectroscopy measurements to estimate the implied SBH from the material energy levels.

S7. Analysis of XPS Result on TiO_2 Samples

The instrument was operated by using Mg line radiation with a probing depth of around 10nm, which depends on the kinetic energy of the electrons emitted from a specific element. With the radiation of X-ray, the electrons are excited and emitted from the core level of atom. The XPS was done in the same ultra-high vacuum (UHV) chamber with UPS thus they were performed in-situ.

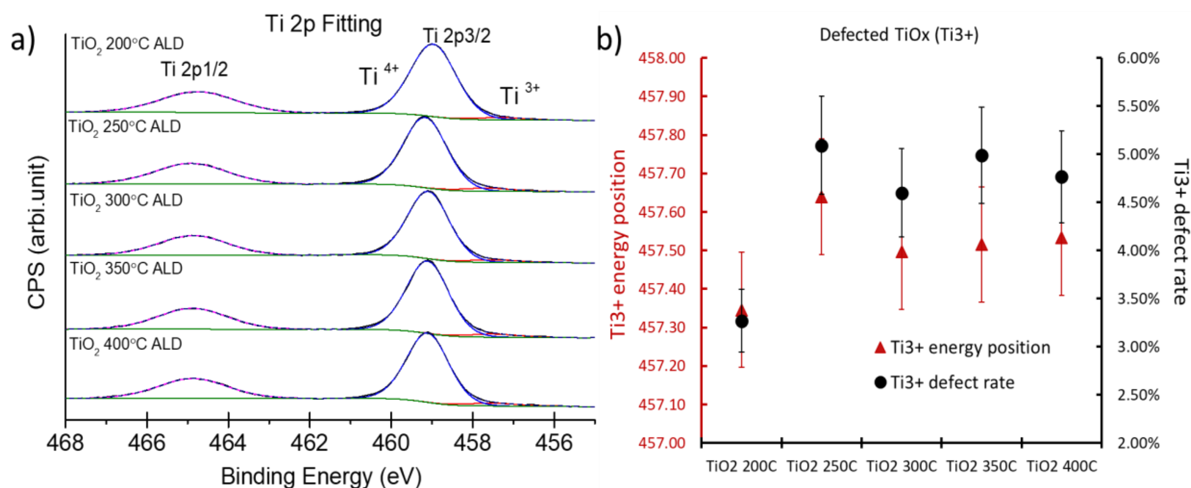

Figure S9 a) Fitting of Ti 2p3/2 and 2p1/2 spectra of samples with various TiO2 ALD deposition temperatures. Ti^{3+} can be observed; b) Energy position of Ti^{3+} and relative intensity of Ti^{3+} defects.

In Figure S9 the fitting of Ti $2p_{3/2}$ leads to the finding of Ti^{4+} (459 ± 0.15 eV) and Ti^{3+} (457.6 ± 0.15 eV) respectively. [11][12] In Figure S9 b), the binding energy position of Ti^{3+} is within the error bar. The defect rate of Ti^{3+} of 250 °C sample peaks over the temperature range. The defect rate from XPS is in line with the finding of electronic states occurring apparently of 250 °C ALD TiO_2. It is important to note that due to the difference of probing depth of XPS and UPS, UPS is more sensitive to surface properties while XPS probes over a depth of approximately 10nm. Therefore, the defected electronic states observed in UPS in relative to other samples is more obvious than the difference of defect rate derived from XPS.

S8. A Verification of the Bandgap Values

The bandgaps of TiO_2 deposited at different temperatures obtained from UV-Vis measurements (Figure S10) are consistent with that from UPS measurements, which could be a verification of the bandgap estimation. The bandgaps from UV-vis have relatively large errors because the data points used for the linear fitting of the curves are chosen manually.

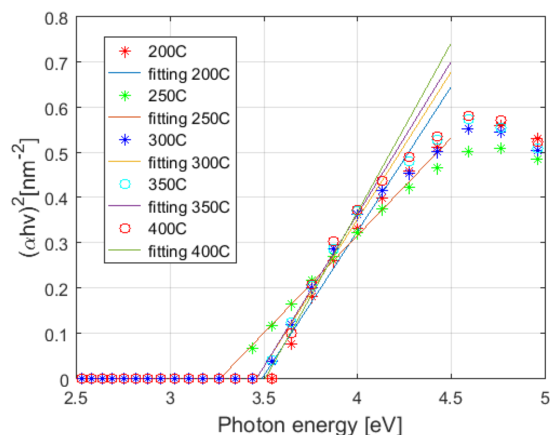

Figure S10 Bandgap from UV-vis as a verification of the bandgap from UPS

S9. Size Distributions of Au NPs

Figure S11 shows the SEM images of NPs and the distributions of particle diameters measured with a custom-built MATLAB image recognition script. The Au NP size on all the TiO_2 layers deposited at different temperatures was 10±4 nm diameter, indicating that the impact of the size of Au NPs on the band alignment at the interfaces in the devices could be ignored.

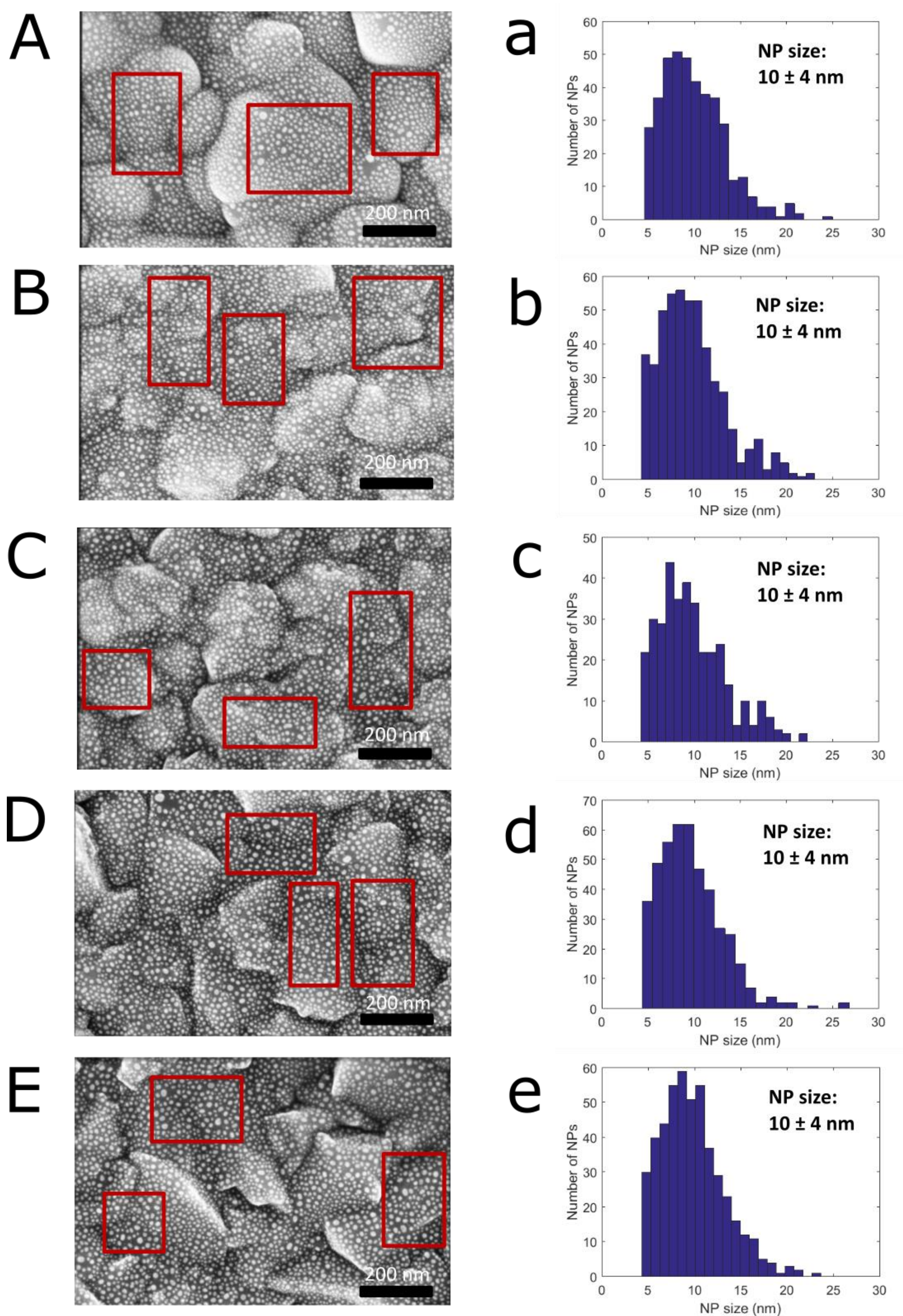

Figure S11 Size distribution of AuNPs on ALD TiO_2 coated FTO. A, B, C, D, E are the SEM images of AuNPs for various TiO_2 ALD deposition temperatures 200 ˚C, 250 ˚C, 300 ˚C, 350 ˚C, 400 ˚C.

Scale: 200 nm. The red rectangles on the SEM images indicate the regions of the films that are used for the statistical calculations of NP size; a, b, c, d, e are the NP size distribution of corresponding SEM images.

S10. Optimization of the Thicknesses of TiO_2 and NiO Layers

Figure S12 shows EQE at resonance as a function of the thickness of TiO_2 as well as NiO layer. The results show that the EQE at resonance of devices with TiO_2 of 25nm is higher than those with thick TiO_2, but more than half of the devices with the thinnest TiO_2 (25nm thickness) are not Schottky diodes that have rectification characteristics. We found that 75nm TiO_2 has a better EQE than 50nm and 100nm TiO_2 at the same ALD processing temperature 300 ˚C. Therefore, 75nm TiO_2 was chosen in this work. It also shows that the EQE at resonance has an overall decrease trend with increasing thickness of the NiO layer from 3nm to 15nm, and 6nm of NiO provides higher and more stable EQE at resonance than the 3nm of NiO. Therefore, 7±1nm NiO was chosen here.

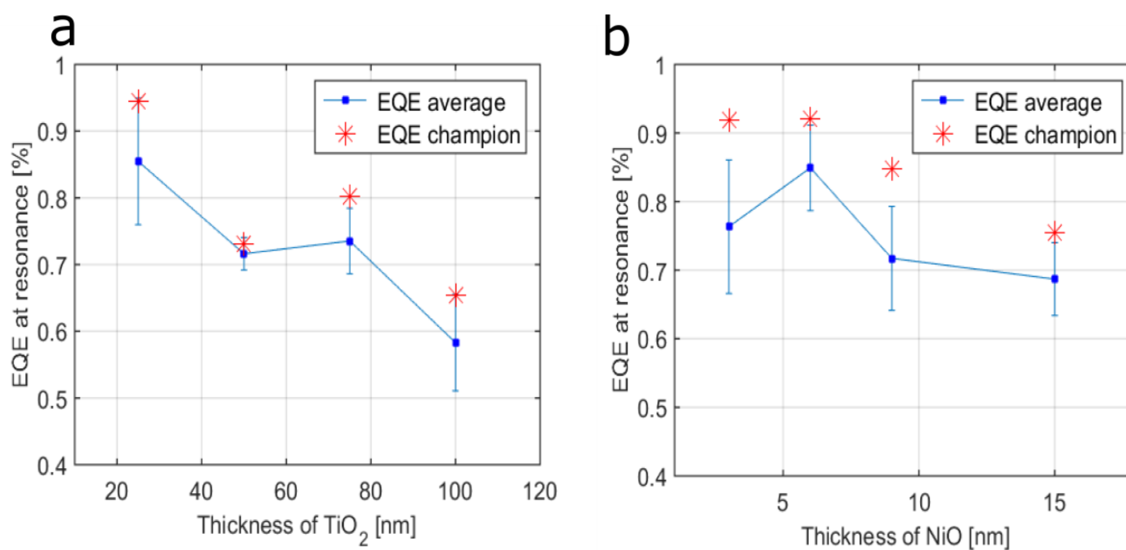

Figure S12 EQE at resonance as a function of TiO_2 and NiO layer thickness

S11. Description of the Calculation for Quantum Yield

We follow the method of Govorov and colleagues to calculate the hot electron generation rate in metal nanoparticles, [13,14] and hence estimate the internal quantum efficiency limits in plasmonically enhanced hot-electron devices (PEH) based on spherical metal nanoparticle absorbers.

Bestiero provides analytical expressions to calculate the hot electron generation rate due to excitation and decay of plasmonic resonances in nanospheres of Au and Ag. [11] In this framework the total absorption in a nanoparticle is split into a classical component and a component due to the generation of hot electrons:

$$Q_{tot} = Q_{hot} + Q_{abs} \tag{1}$$

These quantities are energy dissipation rates with units of $[eVs^{-1}]$. The classical absorption is given in SI units by

$$Q_{Classical} = \epsilon_0 \Im m(\epsilon_M) \frac{\omega}{2}\frac{4}{3}\pi r^3 \left|\frac{3\epsilon_D}{2\epsilon_D + \epsilon_M}\right|^2 \frac{2}{c\epsilon_0\sqrt{\epsilon_D}} I_0 \tag{2}$$

with $\omega = \frac{2\pi c}{\lambda}$ is the free space optical frequency of the incident light with intensity, I_0.

In the quasi-static limit, the rate of energy dissipation due to hot electron generation is given by:

$$Q_{hot} = \frac{1}{4}\frac{2}{\pi^2}\frac{e^2 E_F^2}{\hbar}\frac{1}{(\hbar\omega)^2}\frac{4\pi r^2}{3}\left|\frac{3\epsilon_D}{2\epsilon_D + \epsilon_M}\right|^2 \frac{2}{c\epsilon_0\sqrt{\epsilon_D}} I_0 \tag{3}$$

where $E_F = 5.5\ eV$ is the Fermi energy of gold.

Figure S13 shows the calculated energy dissipation for a spherical Au MNP, with $r = 5\ nm$, surrounded by a dielectric with a constant permittivity of $\epsilon_M = 4$, with an incident light intensity of $I_0 = 1000\ Wm^{-2}$. The classical absorption cross-section (Q_{abs}, blue line), hot electron absorption cross-section (Q_{hot}, red line), and the total absorption cross-section (Q_{tot} , black line) are plotted. The spectra all exhibit a clear peak associated with the plasmonic resonance at a wavelength of 600 nm.

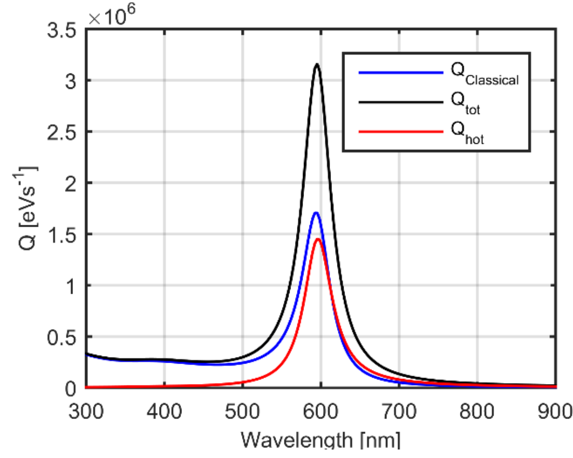

Figure S13 Calculated energy dissipation in a spherical Au MNP, with $r = 5\,nm$*, surrounded by a dielectric with a constant permittivity of* $\epsilon_M = 4$*. The incident light intensity is taken to be* $I_0 = 1000\ Wm^{-2}$ *. Data is shown for classical (*$Q_{classical,}$*blue line), hot electron (*Q_{hot}*, red line) and total absorption cross-section (*$Q_{tot} = Q_{abs} + Q_{hot}$*, black).*

In PEH devices, only some of the generated hot electrons will have enough energy to be injected over the Schottky barrier, with an energy of E_{SBH}. The portion of the energy dissipated due to of 'over-barrier' hot electron generation can be calculated as

$$Q_{ob} = \frac{\hbar\omega - E_{SBH}}{\hbar\omega} Q_{hot} \tag{4}$$

where $\hbar\omega$ is the energy of the photon.

We can define the quantum yield as the fraction of the total energy dissipated in the MNP by absorption that generates over-barrier hot electrons:

$$QY = \frac{Q_{ob}}{Q_{tot}} \tag{5}$$

The quantum yield can be compared directly to measured internal quantum efficiency - i.e. the fraction of absorption photons that are collected and generate current in a device - for an experimental PEH device.

Figure S14 shows the quantum yield for the same MNP as discussed previously, for a range of barrier heights from $E_b = 0 - 1$ eV. The data shows a clear dependence on the Schottky barrier height, as expected, with larger barriers reducing the number of hot electrons that can be injected. This is an absolute upper limit as we are explicitly assuming that all photons that can be absorbed are, and that all over-barrier hot electrons are collected at the contacts.

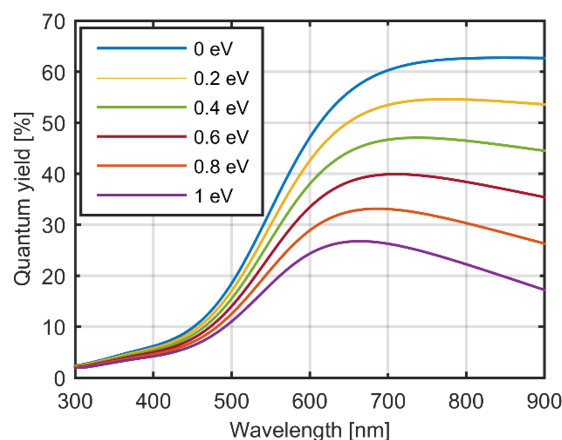

Figure S14 Calculated quantum yield (QY) for over-barrier hot electrons of different Schottky barrier heights.

We directly compare the calculated quantum yield on resonance (defined from the calculated Q spectra in Figure S14 as a wavelength of 600nm) with the experimentally measured IQE on resonance. These results are given in Figure 6 in the main manuscript.

Reference:

[1] S. K. Cheung, N. W. Cheung, *Appl. Phys. Lett.* **1986**, *49*, 85.

[2] V.E. Gora, A. Chawanda, C. Nyamhere, F.D. Auret, F. Mazunga, T. Jaure, B. Chibaya, E. Omotoso, H.T. Danga, S.M. Tunhuma, *Phys. B* **2018**, *535*, 333–337.

[3] M. C. K. Sellers, E. G. Seebauer, *Thin Solid Films* **2011**, *519*, 2103.

[4] A. Eroğlu, S. Demirezen, Y. Azizian-Kalandaragh, Ş. Altındal, *J. Mater. Sci. Mater. Electron*. **2020**, *31*, 14466.

[5] M.S.P. Reddy, K. Sreenu, V.R. Reddy, C. Park, *J. Mater. Sci. Mater. Electron*. **2017**, *28*, 4847.

[6] E.E. Tanrıkulu, S. Demirezen, Ş. Altındal, İ. Uslu, *J. Mater. Sci. Mater. Electron*. **2017**, *28*, 8844.

[7] H.G. Çetinkaya, Ş. Altındal, I. Orak, I. Uslu, *J. Mater. Sci. Mater. Electron*. **2017**, *28*, 7905.

[8] M. C. K. Sellers, E. G. Seebauer, *Thin Solid Films* **2011**, *519*, 2103.

[9] H. Xue, W. Chen, C. Liu, X. Kong, P. Qu, Z. Liu, J. Zhou, **2008**, 108.

[10] N. Szydlo, R. Poirier, *J. Appl. Phys*. **1980**, *51*, 3310.

[11] W. Guan, G. Sun, L. Yin, Z. Zhang, S. Tian, *Front. Chem.* **2018**, *6*, 1.

[12] H. Zhang, X. Shi, A. Tian, L. Wang, C. Liu, *Appl. Surf. Sci.* **2018**, *436*, 579.

[13] L. V. Besteiro, X. T. Kong, Z. Wang, G. Hartland, A. O. Govorov, *ACS Photonics* **2017**, *4*, 2759.

[14] A. O. Govorov, H. Zhang, Y. K. Gun'ko, *J. Phys. Chem. C* **2013**, *117*, 16616.